

Lagrangian Detection of Wind Shear for Landing Aircraft

HOSSEIN AMINI KAFIABAD

Department of Mechanical Engineering, McGill University, Montreal, Quebec, Canada

PAK WAI CHAN

Hong Kong Observatory, Kowloon, Hong Kong, China

GEORGE HALLER

*Department of Mechanical Engineering, McGill University, Montreal, Quebec, Canada,
and Institute for Mechanical Systems, ETH Zurich, Zurich, Switzerland*

(Manuscript received 31 August 2012, in final form 17 June 2013)

ABSTRACT

Recent studies have shown that aerial disturbances affecting landing aircraft have a coherent signature in the Lagrangian aerial particle dynamics inferred from ground-based lidar scans. Specifically, attracting Lagrangian coherent structures (LCSs) mark the intersection of localized material upwelling within the cone of the lidar scan. This study tests the detection power of LCSs on historical landing data and corresponding pilot reports of disturbances from Hong Kong International Airport. The results show that a specific LCS indicator, the gradient of the finite-time Lyapunov exponent (FTLE) field along the landing path, is a highly efficient marker of turbulent upwellings. In particular, in the spring season, projected FTLE gradients closely approach the efficiency of the wind shear alert system currently in operation at the airport, even though the latter system relies on multiple sources of data beyond those used in this study. This shows significant potential for the operational use of FTLE gradients in the real-time detection of aerial disturbances over airports.

1. Introduction

The short-term prediction of disturbances encountered by aircraft in the last minutes of landing provides safer and more comfortable flight for passengers. Here we evaluate the performance of a recently proposed Lagrangian (i.e., particle based) algorithm for the detection of such disturbances using historical landing data and pilot reports from Hong Kong International Airport.

Topography-induced wind shear accounts for about 70% of reported disturbances on landing aircraft at Hong Kong International Airport (HKIA) (Shun and Chan 2008). While radars detect wind shear due to thunderstorms, they may miss high levels of wind shear in nonrainy weather. Such clear-air turbulence, by contrast, is well captured by Doppler lidars currently in operation at HKIA (Shun and Lau 2002; Chan et al. 2006; Shun and Chan 2008).

Lidars measure air velocity from reflections of a laser beam on aerosols using the Doppler effect. Although individual lidar returns only provide line-of-sight velocity components, variational schemes are available to reconstruct full two-dimensional velocity components in the conical surface spanned by the rotating lidar beam (Chan and Shao 2007). This velocity field is updated every 2 min, providing a time-resolved input for automated algorithms that seek to detect aerial turbulence.

One such algorithm locates critical values of the velocity fluctuation, defined as the difference of the measured air velocity from an averaged background velocity (Chan et al. 2006; Chan and Lee 2012). Another approach is based on eddy dissipation rate, an internationally adopted metric for turbulence intensity (Chan 2010). Finally, the autocorrelation of scanned velocity in different sectors has also been employed in wind shear detection (Chan and Lee 2012).

These wind shear detection methods are fundamentally Eulerian, inferring flow features from instantaneous air velocity. As such, they are sensitive to transient errors in velocity measurement and reconstruction. To

Corresponding author address: George Haller, Institute of Mechanical Systems, ETH Zurich, Tannenstrasse 3, CLA J.27, 8044 Zurich, Switzerland.
E-mail: georgehaller@ethz.ch

de-emphasize such errors and anomalies, one may instead look for the signatures of sustained wind shear in the two-dimensional virtual particle dynamics generated by the reconstructed velocity field on the cone of the lidar scan. This Lagrangian averaging approach has been developed in a series of papers by Tang et al. (Tang et al. 2010, 2011a,b), serving as a basis for the present study.

Tang et al. located attracting Lagrangian coherent structures (LCSs)—that is, locally most attracting material lines—in the Lagrangian flow over the lidar cone. They obtained LCSs as select ridges of the backward-time finite-time Lyapunov exponent (FTLE) field, which characterizes the rate of convergence of virtual air particles. These results confirm the ability of backward-time FTLE ridges to pinpoint the location of intense three-dimensional material updrafts between rolling vortices from two-dimensional lidar scans (Tang et al. 2011a). The extracted attracting LCSs were insensitive to instantaneous velocity fluctuations, and correlated well with wind shear jumps measured on landing fixed-wing research aircraft.

Here we present a more systematic study to assess the power of LCS analysis in real-time wind shear detection for commercial aircraft. We analyze roughly 11 months of continuous velocity data from long-range lidars based at HKIA as well as actual pilot reports of wind shear from commercial aircraft during the same period. Using receiver operating characteristic (ROC) graphs, we assess various metrics for the aviation hazard posed by a given LCS. Out of this comparison, the gradient of the FTLE field projected along the runway emerges as a reliable wind shear detection tool, with high hit rates and relatively low alert durations.

For the spring-season part of the available dataset, our FTLE-based wind shear detection scheme is found to compare very favorably with the algorithm currently in operation at HKIA, even though the latter also uses additional information from dedicated short-range glide-path scans and radars. Our method shows consistent but more modest performance for the remaining two seasons. In these seasons, the current operational algorithm prevails because of its additional sources of input, which continue to provide reliable velocity scans in the presence of rain as well.

The organization of this paper is as follows. In section 2, we review the topography of HKIA, its lidar installation, and the dataset used in our study. Section 3 summarizes the main elements of LCS theory and FTLE analysis, and outlines the Lagrangian metrics we test for quantifying the aviation hazard of a given FTLE ridge. In section 4, we employ ROC graphs to evaluate these metrics, and compare them with the wind shear detection scheme

currently in use at HKIA. We present a summary and outlook in section 5.

2. Data used in this study

a. Topography of Hong Kong International Airport

Shown in Fig. 1, HKIA is built on Chek Lap Kok Island, surrounded by ocean on three sides and by Lantau Island to the south. This island has a mountainous terrain, with peaks of 1000 m above sea level. Prevailing easterly winds tend to generate rolling vortices off the peaks, creating major aerial disturbances in the form of updrafts, downdrafts, and close-to-ground planar shear. Indeed, pilot reports recorded at HKIA show that one in about 500 flights experiences significant wind shear (Shun and Chan 2008).

Figure 1 also indicates the location of HKIA's northern runway (25RA) and those of two long-range lidars. A second runway in the southern part of the island is not considered in this study.

b. Lidar scans, reconstructed velocity, and pilot reports

The two long-range lidars at HKIA have been in round-the-clock operation since 2002, providing three types of scans: plan position indicator (PPI) scans, glide-path scans, and vertical scans (Shun and Lau 2002). In a PPI scan, the elevation angle is fixed while the lidar beam performs a full 360° rotation, providing updated velocities every 2 min. To stay close to common flight paths in the last minutes of landing, the scans use the elevation angles 1.4° and 3°.

Figure 2 shows the PPI scan geometry for the northern lidar, whose scans are used in the present study. This lidar operates at a wavelength of 2 μm , with pulse energy of about 2 mJ. Its range resolution of 100 m with 1024 range bins is appropriate for the detection of typical wind shear features, reported to be between 400 m and 4 km in length (Fujita 1978; Proctor et al. 2000; ICAO 2005).

Lidars provide line-of-sight (LOS) velocity components along the rays in their conical span. To reconstruct the two-dimensional projection of the full air velocity field onto the cone of the scan, we use the variational algorithm discussed in Chan and Shao (2007). Our study period comprises historical velocity data from the year 2010 for the following three time intervals:

- 1) *spring*: 1 January–8 April,
- 2) *summer*: 1 May–31 August, and
- 3) *fall*: 1 September–29 November.

We also utilize reports of observed wind shear cases, as recorded at HKIA during our study period. In aviation meteorology, *wind shear* refers to a sustained change

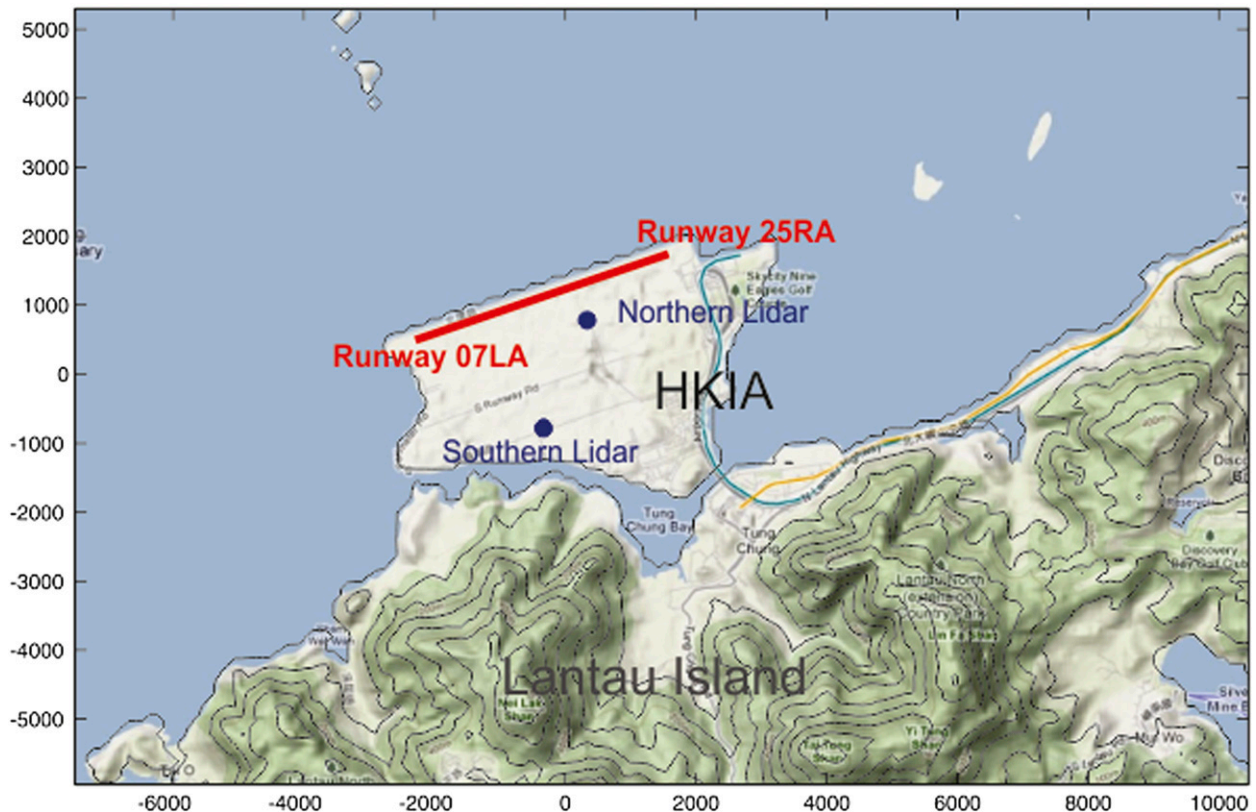


FIG. 1. Topography of HKIA and its surroundings. Also shown are the lidar installations (blue dots) and the runway 25RA (red) considered in this study. Axis unit are in meters; the origin is the midpoint between the two lidars.

(one lasting more than a few seconds) in the headwind or tailwind of the aircraft. Conventionally, a velocity change of 15 kt ($1 \text{ kt} = 0.51 \text{ m s}^{-1}$) or more is considered significant wind shear. In our study period, the following numbers of significant wind shear were reported by pilots for runway 25RA: spring: 79 reports; summer: 90 reports; fall: 38 reports.

Since rain is known to negatively impact lidar performance, the amount of continuously available velocity data in a given season correlates with the amount of clear days in that season. As a result, all three study periods contain time periods (ranging from minutes to a couple of days) with no reliable lidar scans because of rain. Another cause for missing data was lidar component malfunction. All in all, the highest-quality data were available for the spring period, but we did carry out our study for the summer and fall periods to uncover any potential significant seasonal dependence in our analysis.

3. LCS analysis

a. Mathematical setup

Particles advected under a three-dimensional velocity field $V = (u, v, w)$ satisfy the following equation of motion:

$$\dot{X} = V(X, t), \quad (1)$$

with $X(t) \in \mathbb{R}^3$ denoting particle positions at time t . Even in steady flows, the Lagrangian structures organizing the behavior of particles can have complex geometry, leading to chaotic trajectories (Ottino 1997). Lagrangian dynamics in time-periodic flows are equally or more complicated, but they can at least be efficiently visualized via the iteration of Poincaré maps—that is, stroboscopic pictures of the trajectory evolution taken at multiples of the time period. Both for steady flows and Poincaré maps, stable and unstable manifolds of fixed points are known to be the organizing centers for evolving tracer patterns (Ottino 1997).

By contrast, visualizing the organizing centers of Lagrangian behavior in temporally aperiodic flow data is a challenge. LCSs have been found to form such centers, providing a generalization of stable and unstable manifolds for nonperiodic flows. Attracting LCSs are locally the most attracting material surfaces in the flow, along which tracer blobs elongate in forward time (Haller 2001). Similarly, repelling LCSs are locally most repelling material surfaces, acting as dividing lines between regions of different particle behavior.

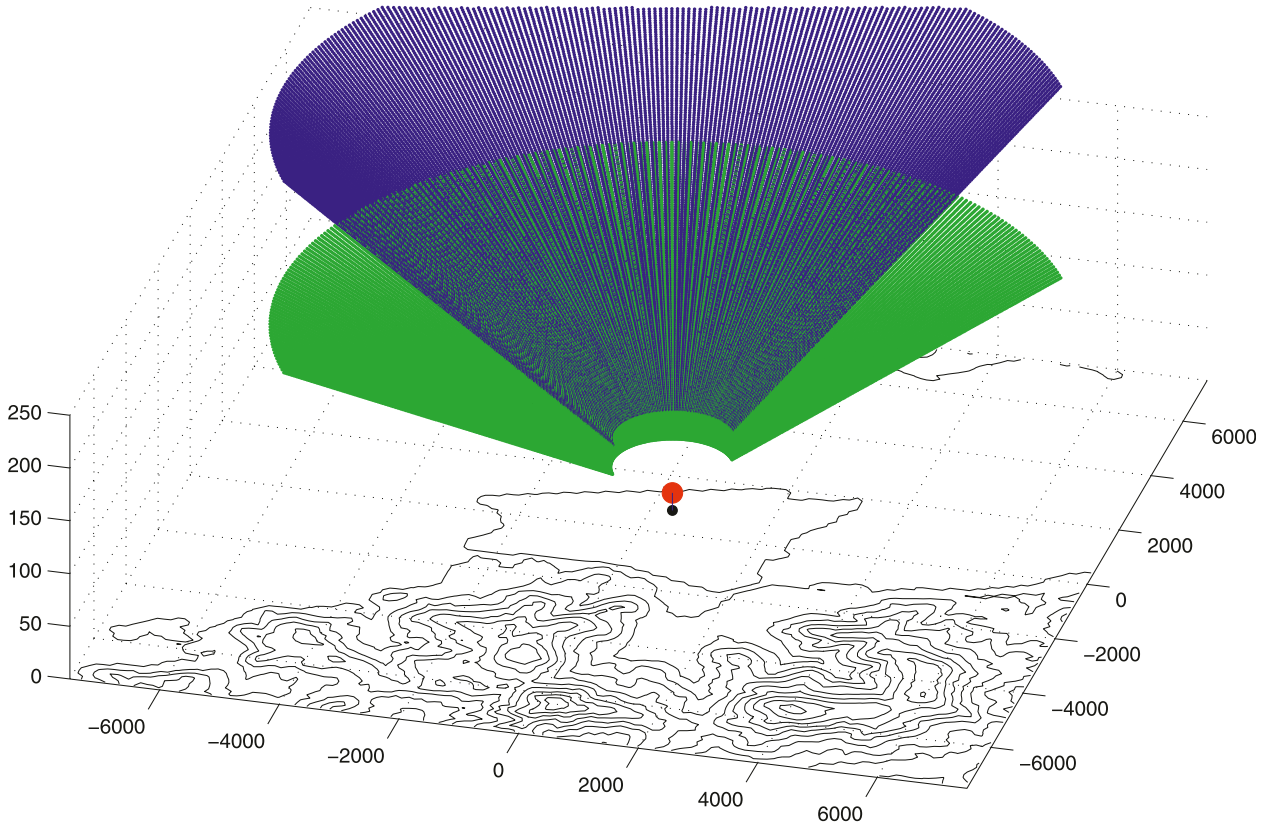


FIG. 2. Geometry of scans by the northern lidar at HKIA, with elevation angles of 1.4° (green) and 3° (blue). All spatial dimensions are in meters, with the origin of the coordinate system based at the midpoint between the two lidars. For better visibility, only parts of the full conical scans are shown.

Mathematical theories and numerical methods for detecting LCSs have been constantly improving (Peacock and Dabiri 2010). The currently most advanced methods take a variational approach, providing high detail but also requiring high spatial resolution in the velocity data (Haller 2011; Haller and Beron-Vera 2012). Here we detect LCSs from FTLEs, which are well suited to handle the relatively low spatial and temporal resolution of the available lidar scans.

The conical scans are well approximated as planes due to their low-elevation angles. In this approximation, we replace the full 3D air velocity field $V(X, t)$ with a two-dimensional planar field:

$$\dot{\mathbf{x}} = \mathbf{u}(\mathbf{x}, t), \tag{2}$$

with $\mathbf{u} = (u, v)$, $\mathbf{x} = (x, y)$. The flow map $F_{t_0}^t(\mathbf{x}_0) = \mathbf{x}(t; t_0, \mathbf{x}_0)$ associated with (2) maps initial positions \mathbf{x}_0 at time t_0 to the later positions $\mathbf{x}(t; t_0, \mathbf{x}_0)$ at time t along trajectories of (2). As such, $F_{t_0}^t(\mathbf{x}_0)$ describes a projected virtual flow, because real air particles do not remain confined to the lidar cones. We use this virtual flow to average out anomalies from the velocity field, and

locate the intersection of three-dimensional LCSs with the lidar cones.

We start by computing the *Cauchy–Green strain tensor field*:

$$C_{t_0}^t = [\nabla F_{t_0}^t]^* \nabla F_{t_0}^t, \tag{3}$$

with $[\cdot]^*$ denoting matrix transposition. At each initial position \mathbf{x}_0 , the eigenvectors $\xi_i(\mathbf{x}_0)$ of the positive definite tensor $C_{t_0}^t(\mathbf{x}_0)$ satisfy $C_{t_0}^t \xi_i = \lambda_i \xi_i$, with the strain eigenvalues $\lambda_i(\mathbf{x}_0)$ ordered as $\lambda_2 \geq \lambda_1 > 0$. The rate at which trajectories of (2) diverge from each other is measured by the FTLE field as shown:

$$\Lambda_{t_0}^t(\mathbf{x}_0) = \frac{1}{|t - t_0|} \log \|\nabla F_{t_0}^t(\mathbf{x}_0)\| = \frac{1}{2|t - t_0|} \log \lambda_2(\mathbf{x}_0, t_0, t). \tag{4}$$

Recent results show (Haller 2011; Tang et al. 2011b; Farazmand and Haller 2012) that ridges of the FTLE field computed in backward time (i.e., for $t < t_0$) mark attracting LCSs if they are approximately normal to the dominant strain eigenvector field $\xi_2(\mathbf{x}_0)$. Computations

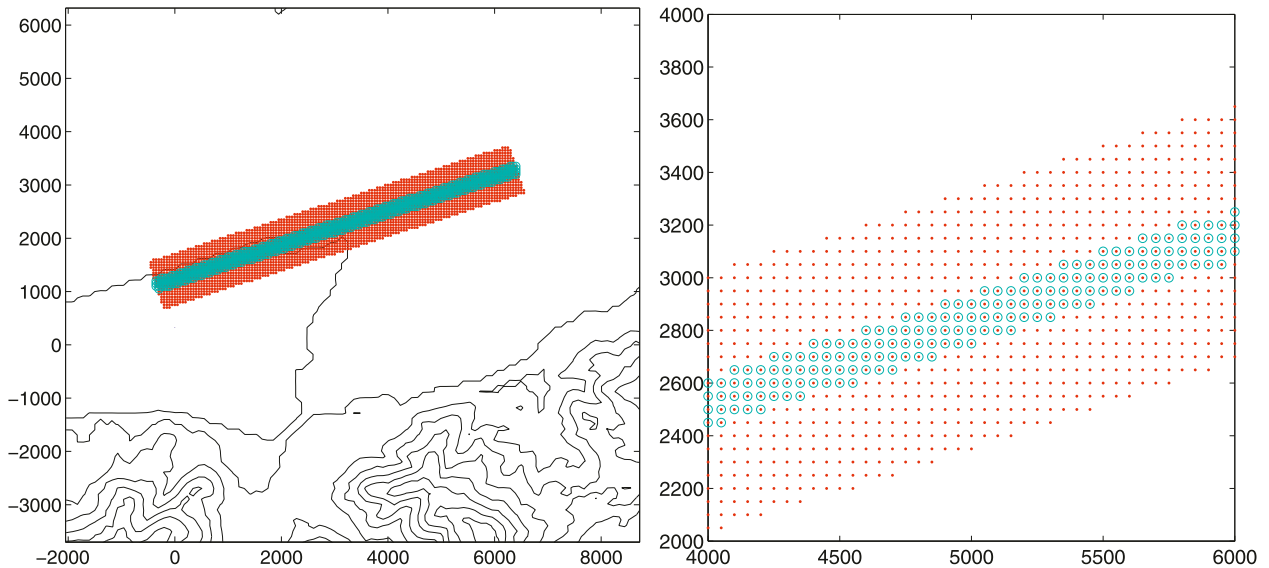


FIG. 3. (left) Computational domain near runway 25RA. Red dots denote the initial grid domain for FTLE calculations. Within this, cyan dots mark the domain for LD. Units are in meters. (right) Magnified computational grid containing the initial conditions \mathbf{x}_0 for the functions $\Lambda_{t_0}^t(\mathbf{x}_0)$ and $LD_{t_0}^t(\mathbf{x}_0)$.

in Tang et al. (2011b) confirmed that most LCSs relevant in the detection of updrafts at HKIA tend to satisfy this near-orthogonality condition. The low number of FTLE ridges not satisfying the near-orthogonality condition corresponds to horizontal shear, which may impose a horizontal jolt on landing aircraft. Here we only focus on identifying the FTLE ridges accurately and assessing the level of aviation hazard they pose.

An alternative indicator for three-dimensional attracting material structures is the Lagrangian divergence:

$$LD_{t_0}^t(x_0) = \frac{1}{|t - t_0|} \int_{t_0}^t \mathbf{v} \cdot \mathbf{u}[\mathbf{x}(s; t_0, \mathbf{x}_0), s] ds, \quad (5)$$

computed along trajectories of (2). As argued in Tang et al. (2011a,b), large values of $LD_{t_0}^t(x_0)$ necessarily signal significant three-dimensional stretching or compression, given that the full three-dimensional velocity field (1) is practically incompressible. Accordingly, in low-altitude scans, large negative values of $LD_{t_0}^t(x_0)$ indicate highly localized updrafts, with air particles being sucked into the updraft along horizontal directions. Similarly, large positive values of $LD_{t_0}^t(x_0)$ obtained from low-angle lidar scans indicate localized downdrafts, with air particles leaving the location of the downdraft along horizontal directions.

b. Computation of LCSs

The two-dimensional velocity field (2), reconstructed from LOS velocities via the variational algorithm of Chan and Shao (2007), is available on a Cartesian grid of

15 km \times 15 km, centered at the midpoint between the two lidars shown in Fig. 1.

We calculate the FTLE distribution $\Lambda_{t_0}^t(\mathbf{x}_0)$ and the Lagrangian divergence distribution $LD_{t_0}^t(x_0)$ from initial particle positions \mathbf{x}_0 seeded along runway 25RA, as shown in Fig. 3. These initial grids include the runway and part of a typical flight path during the last few minutes of landing. Integrating the differential (2) between a current time t_0 and a past time $t < t_0$, for all points \mathbf{x}_0 in the initial grid, yields a discrete approximation for the backward-time flow map $F_{t_0}^t(\mathbf{x}_0)$. We carry out this integration using a variable step size Runge–Kutta method.

The end time of backward integration is $t = t_0 - 300$ s for each present time t_0 . Given that the velocity field is updated every 2 min, about three scans are used in each advection. We have found empirically that this time scale is short enough to reveal transient Lagrangian effects while still yielding well-pronounced FTLE ridges. Trajectories leaving the computational domain during the integration are advected further by a smooth, linear, and divergence-free extension of the original velocity field. As shown in Tang et al. (2010), this method eliminates artificial FTLE ridges created by edge effects that arise if trajectories are stopped at the boundary.

We apply finite differencing to the discretized $F_{t_0}^t(\mathbf{x}_0)$ field to obtain the Cauchy–Green strain tensor field $C_{t_0}^t(\mathbf{x}_0)$, as defined in (3). For each initial position \mathbf{x}_0 , the dominant strain eigenvalue $\lambda_2(\mathbf{x}_0)$ is computed explicitly from the entries of the matrix $C_{t_0}^t(\mathbf{x}_0)$. The FTLE field $\Lambda_{t_0}^t(\mathbf{x}_0)$ and the Lagrangian divergence field $LD_{t_0}^t(x_0)$ are

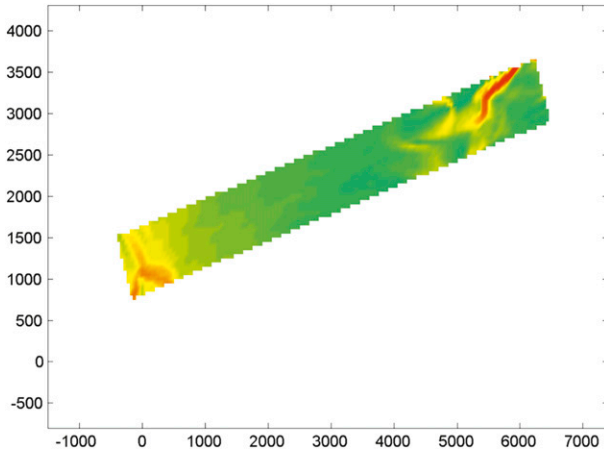


FIG. 4. A sample FTLE distribution over the initial grid shown in Fig. 3.

then obtained as defined in (4) and (5), respectively. A sample result for the FTLE field is shown in Fig. 4.

c. Lagrangian and Eulerian metrics for wind shear intensity

The FTLE field $\Lambda_{t_0}^t(\mathbf{x}_0)$ measures the average exponential rate of separation that nearby air particles exhibit in the flow (2). An airplane flying in a uniform strain or shear field would not experience aerial disturbance, no

matter how high the corresponding uniform FTLE fields were. Instead, we expect jolts on the aircraft to correlate with sharp inhomogeneities (steep ridges) in the backward-time FTLE field, which mark highly localized updrafts.

Correspondingly, $|\nabla\Lambda_{t_0}^t(\mathbf{x}_0) \cdot \mathbf{e}|$, the length of the projection of $\nabla\Lambda_{t_0}^t(\mathbf{x}_0)$ onto the unit vector \mathbf{e} aligned with the glide path, should be a relevant measure of the wind shear experienced by landing aircraft. Figure 5 supports this point by comparing a case of no reported wind shear (left) to a case of reported wind shear (right). In both cases, backward-time FTLE ridges with comparable $\Lambda_{t_0}^t(\mathbf{x}_0)$ and $|\nabla\Lambda_{t_0}^t(\mathbf{x}_0)|$ values intercept the glide path, while their angles with the glide path (and hence the magnitude of $|\nabla\Lambda_{t_0}^t(\mathbf{x}_0) \cdot \mathbf{e}|$) are markedly different. In the second case, the near-orthogonal FTLE ridges generate high $|\nabla\Lambda_{t_0}^t(\mathbf{x}_0) \cdot \mathbf{e}|$ values. Indeed, in this case, high levels of wind shear leading to a missed approach were reported.

While the two events shown in Fig. 5 confirm basic intuition, we will still assess the efficacy of $\Lambda_{t_0}^t(\mathbf{x}_0)$, $|\nabla\Lambda_{t_0}^t(\mathbf{x}_0)|$, and $|\nabla\Lambda_{t_0}^t(\mathbf{x}_0) \cdot \mathbf{e}|$ as wind shear indicators more systematically, by evaluating them on the entire spring dataset, the best-quality part of our full dataset.

We further compare these FTLE-based indicators to $|\text{LD}_{t_0}^t(\mathbf{x}_0)|$ as well as to a common Eulerian metric for wind shear, the jump in nearby velocities along the glide

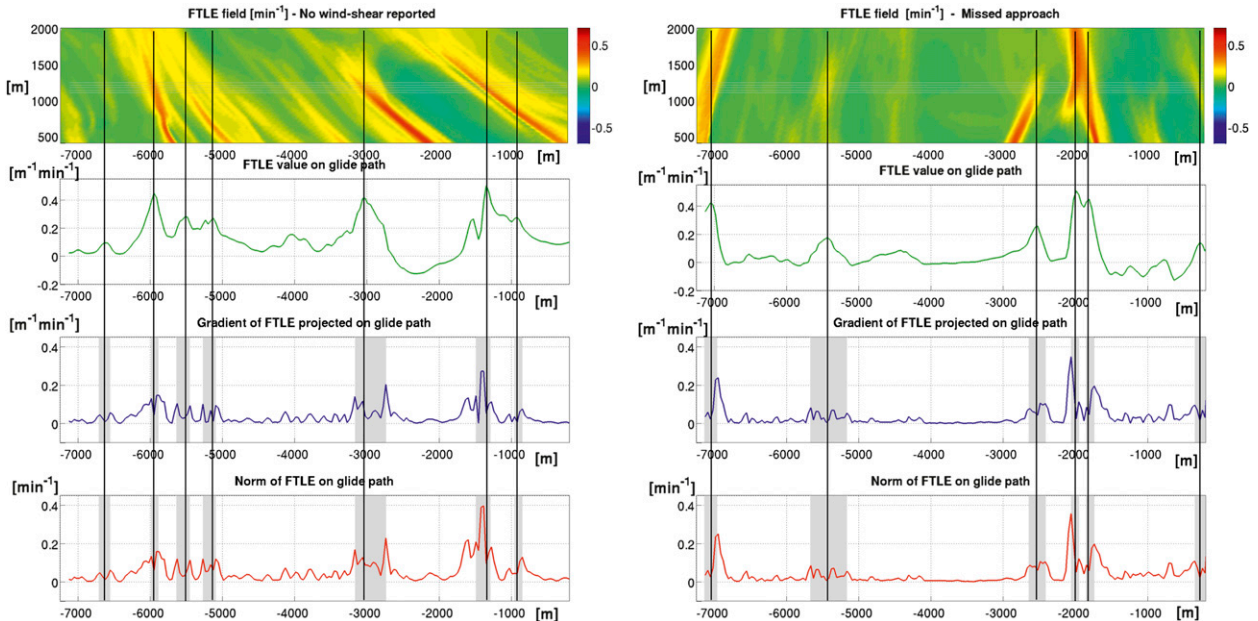


FIG. 5. (left) FTLE distribution at 1222 UTC 2 Feb 2010, when no wind shear was reported. (Parallel horizontal lines on the FTLE plot indicate a typical glide path.) Note how projection on the glide path reduces the peak in the FTLE gradient along the rightmost ridge that encloses a small angle with the flight path. (right) As in (left), but for 1718 UTC 8 Feb 2010, when a missed approach due to wind shear was reported. Note how projection onto the glide path preserves the high peak in the FTLE gradient at ridges that are nearly orthogonal to the flight path.

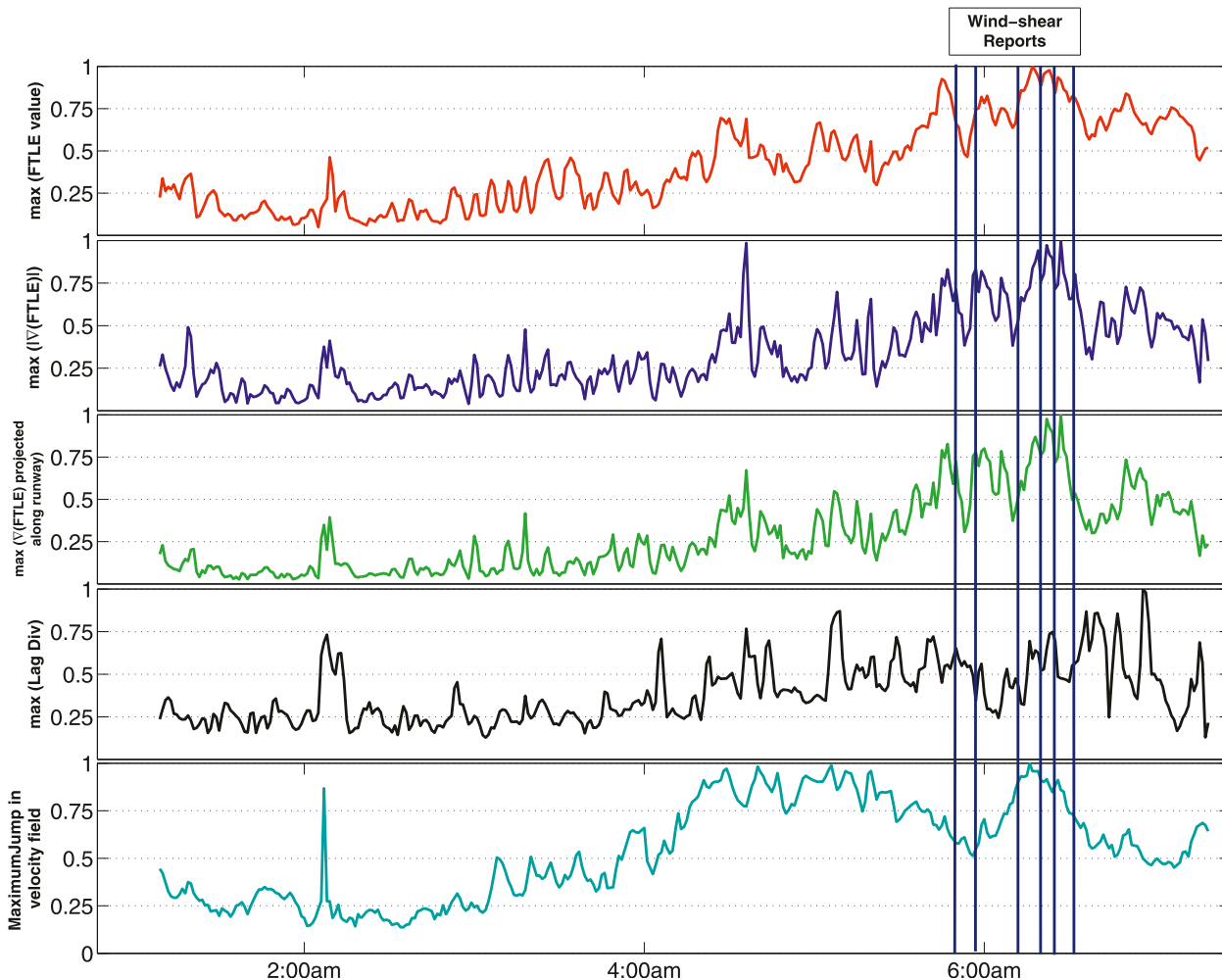


FIG. 6. Time evolution of the normalized maximum values of (top to bottom) Lagrangian and Eulerian metrics along the glide path, including a period of repeated wind shear reports on 15 Jan 2010. (All quantities are normalized by their maximum values within the time interval considered.)

path (Haynes 1980; Jones and Haynes 1984). For this Eulerian metric, let GP denote the glide path (a 7-km-long line) with the fixed orientation defined by the unit vector \mathbf{e} . Then the velocity jump distribution $j(\mathbf{x}_0, t; h)$ is defined as the velocity difference between a point $\mathbf{x}_0 \in$ GP and the point that is in a distance h away from \mathbf{x}_0 in the direction of \mathbf{e} :

$$j(\mathbf{x}_0, t; h) = |[\mathbf{u}(\mathbf{x}_0 + h\mathbf{e}, t) - \mathbf{u}(\mathbf{x}_0, t)] \cdot \mathbf{e}|.$$

If $\mathbf{x}_0 + h\mathbf{e}$ falls outside the actual length of the glide path, then we set $j(\mathbf{x}_0, t; h) = 0$. The *velocity jump metric* is then obtained by taking the maximum of $j(\mathbf{x}_0, t; h)$ over all $\mathbf{x}_0 \in$ GP, and over all ramp lengths h in the set:

$$H = \{100 \text{ m}, 200 \text{ m}, 400 \text{ m}, 800 \text{ m}, 1600 \text{ m}, 3200 \text{ m}\};$$

$$\Delta v(t) = \max_{h \in H} \max_{\mathbf{x}_0 \in GP} j(\mathbf{x}_0, t; h).$$

A version of this velocity jump metric is currently implemented on glide-path scans in the Lidar Wind Shear Alerting System (LIWAS) algorithm at HKIA (Shun and Chan 2008).

Figure 6 shows a comparison of the various wind shear metrics on data from the early morning hours of 15 January 2010. These time series illustrate that Lagrangian metrics are insensitive to isolated, instantaneous jumps in the velocity field. All FTLE-based criteria show good performance, peaking near the wind shear reports and staying near zero otherwise.

We discuss a more systematic evaluation of these metrics over the full dataset in the next section.

4. Performance comparison for wind shear metrics

We evaluate the Lagrangian and Eulerian wind shear metrics discussed in section 3 using the spring, summer,

and fall datasets described in section 2b. For all times and for each metric, we generate a 5-min wind shear alert if the given metric returns a maximum value exceeding a critical threshold (*model parameter*) over the glide path.

a. Definition of ROC graphs

We consider a wind shear metric to perform well if its model parameter can be tuned to yield a high number of hits and a low number of misses. To quantify the performance of each metric we use ROC graphs, following the terminology and convention introduced by Fawcett (2006). To this end, we define the following four cases in our detection:

- 1) *True positive*: The pilot reported wind shear and there was a 5-min alert in effect some time during the landing.
- 2) *True negative*: The pilot reported no wind shear and there was no 5-min alert in effect any time during the landing.
- 3) *False positive*: The pilot reported no wind shear, but there was a 5-min alert in effect some time during the landing.
- 4) *False negative*: The pilot reported wind shear, but there was no 5-min alert in effect any time during the landing.

The two classic quantities used in assessing a particular detection scheme are the following:

$$\text{hit rate} = \frac{\text{true positives}}{\text{true positives} + \text{false negatives}}, \quad (6)$$

$$\text{false alarm rate} = \frac{\text{false positives}}{\text{false positives} + \text{true negatives}}. \quad (7)$$

The ROC graph of a wind shear metric is obtained by plotting the hit rate as a function of the false alarm rate for each tested value of the model parameter. The resulting graph shows the trade-off between benefits (hit rate) and costs (false alarm rate), enabling a comparison between different wind shear metrics, and the optimization of the model parameter for each metric under various performance objectives.

In our study, negative instances would be obtained from null reports—that is, pilot reports of wind shear not exceeding 15 kt. In practice, however, pilots rarely report the lack of wind shear after an uneventful landing, which results in an artificially low number of null reports. This necessitates a modification in the ROC curve: we replace the false alarm rate with the *alert duration* as the independent variable of the graph (Chan and Lee 2012). The alert duration is defined as the percentage of time in

which a wind shear alert would have been generated by the given wind shear metric. This is just the sum of 5-min windows around wind shear alerts, expressed as a percentage of the length of the total study period. Using alert duration instead of the false alarm rate eliminates the issue caused by the lack of a statistically significant number of null reports.

b. Computation of ROC graphs

For each wind shear metric introduced in section 3c, we compute the metric along the flight path for the 5-min window before each reported wind shear event. If, within these 5 min, the value of the metric exceeds the model parameter, then the wind shear report (instance) is marked as a true positive. The total number of these true positives divided by the total number of wind shear reports in the study period gives the hit rate, as defined in (6).

For alert duration, we calculate each metric in every minute of the entire study period (this is achieved by linearly interpolating between two actual lidar scans, which are 2 min apart). If the value of the metric exceeds the model parameter, then a wind shear alert is generated for the following 5 min. The alert duration is then obtained as the total length of these 5-min alerts divided by the length of the entire study period.

For each metric, these computations yield a single point of the ROC graph for a fixed value of the model parameter. Varying the model parameter of the metric and recomputing the hit rate and alert duration will yield further points in the graph. To restrict the analysis to feasible values of the model parameter, we normalize each metric by the historical mean of its maximal values (computed for the given season) during each landing event. This historical mean of maxima is extracted from an initial *sample period*, the first two weeks of our study period. After normalization by this mean, we only vary the model parameter for each metric in the $[0, 1]$ interval.

The historical means of maxima obtained in this fashion for the spring are as indicated in Table 1 (with bars referring to spatially averaged values along the glide path and with the gradients nondimensionalized by the length of the runway).

c. Results

Figure 7 shows the ROC graphs obtained by evaluating our metrics over the summer period (from 1 January to 8 April 2010), containing 79 reported cases of wind shear. As seen in the figure, FTLE-based metrics outperform Lagrangian divergence (LD) in the detection of aerial disturbances. This extends the conclusions of Tang et al. 2011b (established for vertical accelerations on fixed-wing research aircraft from 20 data points) to

TABLE 1. Historical means of maxima for various wind shear metrics.

FTLE	FTLE gradient	PFG	LD	Velocity jump
$\overline{\Lambda_{t_0}^t}$	$\ \overline{\nabla(\Lambda_{t_0}^t)}\ $	$ \overline{\nabla(\Lambda_{t_0}^t)} \cdot \mathbf{e} $	$\overline{LD_{t_0}^t}$	$\overline{\Delta v(t_0)}$
0.6133	113.824	92.261	0.0076	5.5157 (m s ⁻¹)

over 3 months of actual pilot reports from commercial aircraft. Indeed, LD maxima can only mark three-dimensional stretching, whereas FTLE ridges can also be created by two-dimensional strain or shear, both of which may produce jolts on landing aircraft.

Notably, the performance of the Eulerian velocity jump metric is the weakest among all metrics considered, even though it mimics the highly effective glide-path shear alert generation algorithm (GLYGA) currently in operation at HKIA. The reason for this discrepancy is that GLYGA has been developed and optimized for dedicated glide-path scans. By contrast, the velocity jump algorithm used here is implemented on PPI scans that

deviate from actual flight paths. The poor performance of the velocity jump algorithm in our setting underlines the robustness of Lagrangian detection methods, which perform well even on PPI scans.

Within the class of FTLE-based metrics plotted in Fig. 7, the projected FTLE gradient emerges as the statistically most efficient wind shear indicator. This is in agreement with our discussion in section 3c, extending our conclusions from the single daily time series of Fig. 6 to the entire spring period.

For comparison, the brown triangle in Fig. 7 marks the current working point of the GLYGA, computed for the spring period. With an alert duration of 2.5% and a hit rate of 68.9%, this algorithm is currently used in the operational wind shear alerting system at Hong Kong International Airport (Chan and Lee 2012). In addition to detecting velocity jumps from long-range lidar scans, the well-tested and optimized GLYGA also incorporates dedicated glide-path scans as well as scans from ground-based radars.

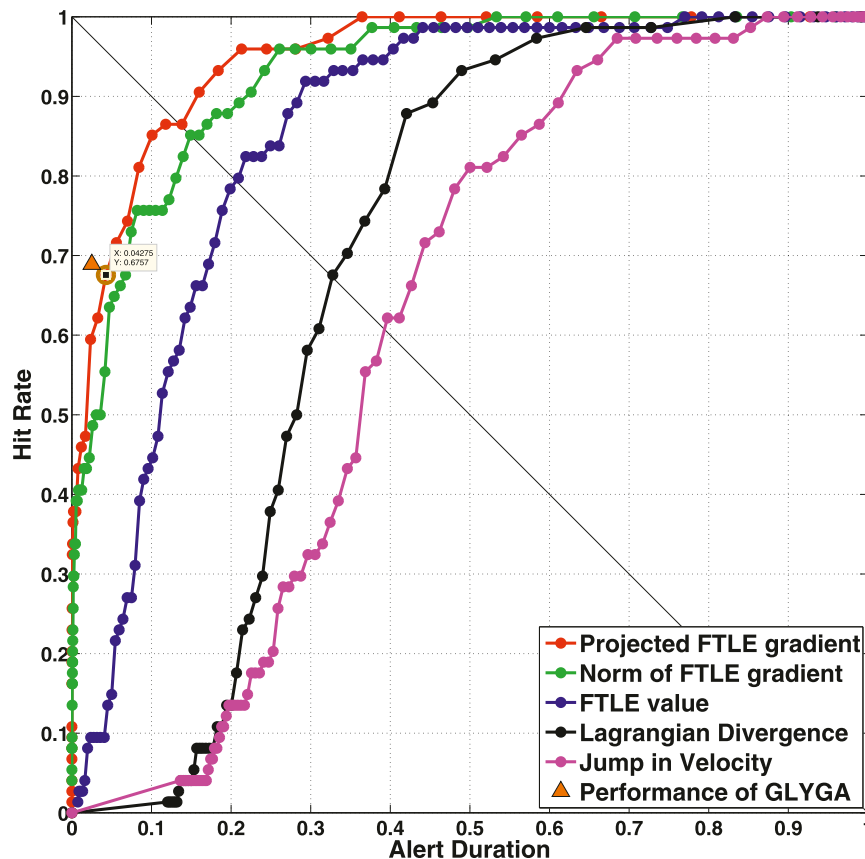


FIG. 7. ROC graphs derived for the spring study period (3 months and 8 days, starting from 1 Jan 2010). The brown triangle marks the performance of the GLYGA, currently in operational use at HKIA. The brown circle shows the closest point obtained from the PFG metric. The corresponding dimensionless model parameter is 39.67.

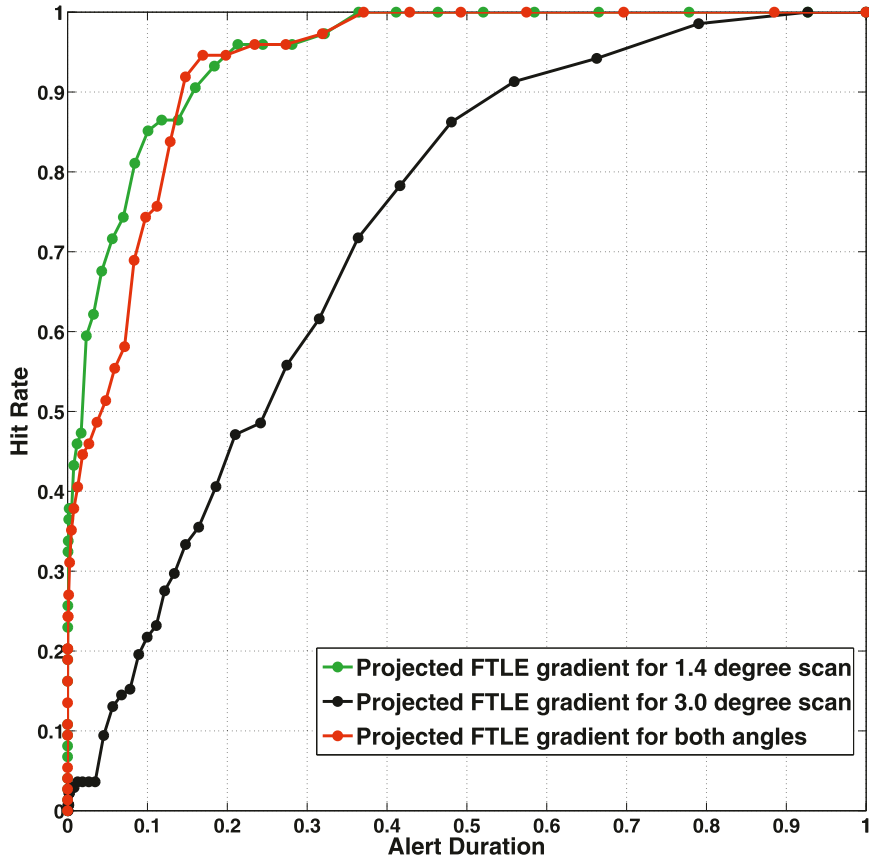


FIG. 8. The performance of the PFG metric, $|\nabla(\Lambda_{t_0}^t) \cdot \mathbf{e}|$, for the scanning angles 1.4° and 3.0° as well as for their combination (for the latter, both scans must be over the same threshold to trigger a wind shear alert).

In the absence of more specific performance objectives, a natural choice for our optimal model parameter value is the one that produces the ROC graph point closest to the current operating point of the GLYGA at HKIA. In Fig. 7, this closest point is encircled, with an alert duration of 4.2% and a hit rate of 67.6%. The corresponding model parameter (i.e., nondimensionalized critical threshold for $|\nabla(\Lambda_{t_0}^t) \cdot \mathbf{e}|$) is 39.67.

Remarkably, the *projected FTLE gradient* (PFG) algorithm developed here produces performance levels closely approaching that of the operational GLYGA. The latter algorithm has been optimized for years, and relies on additional measurements (glide-path scans, radar scans, and anemometer readings) unavailable for our study.

Finally, in Fig. 8, we compare the ROC curves for the PFG algorithm for the scanning angles 1.4° and 3.0° . In the same figure, we also show the ROC curve for a simple combined PFG algorithm that monitors both scans, and triggers an alert if the PFG exceeds the model parameter in either scan.

We conclude from Fig. 8 that the PFG algorithm applied to the 1.4° scan gives significantly better performance than the 3° scan. This result is expected, because lower-angle scans are closer to typical flight paths, and hence will be more in sync with pilot reports. In addition, updrafts between two rolling vortices generate more pronounced attracting LCSs in lower-angle scans, given the intense convergence of particles near the ground [cf. Tang et al. (2011b) for a more detailed description of the three-dimensional geometry of such updrafts].

Also shown in Fig. 8, the quality of the PFG metric computed from both scanning angles approaches and ultimately surpasses that of the 1.4° scan for increasing alert durations. A combined PFG metric with different threshold parameters for each scanning angle might ultimately outperform the 1.4° scan across the board, but the design of such a metric will not be pursued in our present study.

Given the above-mentioned findings for the best-quality spring data period, we focus our study on FTLE-based detection metrics and 1.4° scans for the somewhat

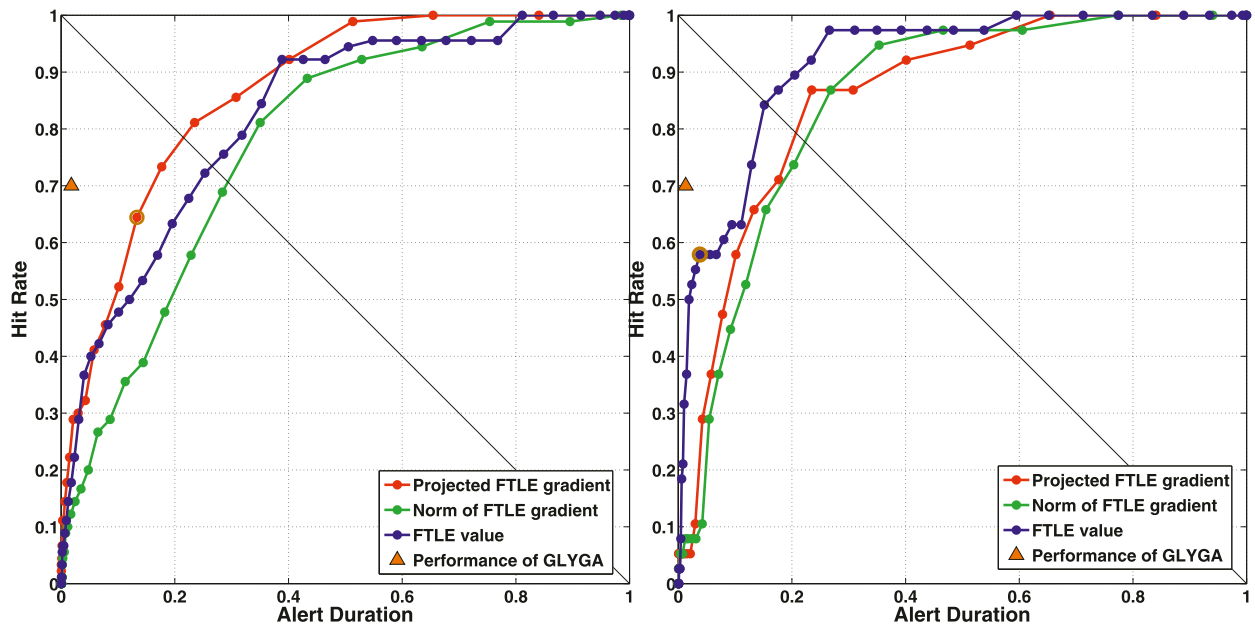


FIG. 9. ROC graphs derived for the summer and fall study periods. Again, brown triangle marks the performance of the operational GLYGA detection algorithm at HKIA. Brown circles show the closest point obtained from the PFG and maximum FTLE metrics, respectively. The corresponding dimensionless model parameters are 16.0 and 0.374, respectively.

lower-quality summer and fall datasets. In each of these datasets, we had intervals of no coverage totaling more than 3 days. Missing data intervals longer than 10 min were left out of the analysis. Those lasting less than 10 min were handled by interpolation from available scans.

The results for these datasets are shown in Fig. 9. We conclude that the efficiency of our PFG algorithm relative to the current operational algorithm at HKIA was slightly lower in the summer than in the spring dataset. The efficacy further decreases in the fall data, with the somewhat surprising emergence of the FTLE maximum as the best metric. Overall, lidar-based Lagrangian wind shear detection shows the highest accuracy for the spring period. The performance of two remaining seasons are also promising, given that no additional velocity data beyond lidar scans was used in these alerts.

The results of Figs. 7 and 9 are better understood in the context of regional climate. The spring season in Hong Kong is relatively dry, securing mostly reliable operating conditions for lidars. While fog spreads often from the South China Sea along eastern and southeasterly winds, these winds are blocked by Lantau Island, leaving the skies over the airport clear. The resulting high viewing quality for lidar scans is clearly reflected in the performance of our algorithm over the spring dataset. By contrast, the summer section of the data fully overlaps with Hong Kong's rainy season, which starts in May and ends in September. Degraded lidar performance due to frequent rain in this period explains the somewhat

weaker performance of our algorithm on the summer data. Finally, the weakest performance in the dry months of October and November should be due to the low number of wind shear reports available from this period. This is expected to weaken the ability of ROC to assess the performance of our algorithm reliably.

5. Conclusions

Using over three seasons of historical data from Hong Kong International Airport (HKIA), we have assessed the power of Lagrangian coherent structure (LCS) analysis in detecting aerial turbulence for landing aircraft. The data used include 11 months of time-resolved long-range lidar scans over runway 25RA as well as time-stamped reports of 207 significant wind shear events reported by pilots in the same period.

We have found that the projection of the gradient of the finite-time Lyapunov exponent (FTLE) field along the runway is an efficient metric for quantifying the LCS signature of reported aerial disturbances. Specifically, calling a wind shear alert when the projected FTLE gradient (PFG) exceeds a critical threshold value, we achieve a historical hit rate of 67.6% over an alert duration of 4.2% for our *spring* study period. For the *summer*, the same approach yielded a hit rate of 65% over a 13.0% alert duration. In the *fall* season, FTLE magnitude emerged as the leading indicator, yielding a more modest 58% hit rate, but from a very short 3.8% alert duration.

For the spring season, the current operational algorithm at HKIA produced only a slightly higher hit rate of 68.9% over a slightly lower alert duration of 2.5%. This operational algorithm, however, also incorporates multiple sources of input, including dedicated scans along the glide path, radar scans, and anemometer readings. These additional inputs all act to mitigate the effect of lidar equipment failure and rain. Given that the present study did not benefit from these inputs, our results show significant potential for the PFG algorithm.

Parallel to lidar measurements, HKIA also operates an anemometer-based wind shear-alerting system called Anemometer-Based Wind shear Alerting Rules—Enhanced (AWARE). With an alert duration of 0.4%, AWARE reached a hit rate of 26% over the period of January–November 2010. This low value indicates the strength of lidar-based wind shear assessment technologies over anemometer-based ones.

Improvements to the PFG algorithm are mainly expected from more frequent and more accurate velocity updates. Indeed, the current scanning frequency of 2 min misses short-term turbulent features that have recently been observed from short-range lidar scans targeting the glide path (Chan and Lee 2012). Further increase in the frequency of velocity updates is expected from future advances in lidar technology, from the deployment of several lidars at the same time and from backup velocity scans from radars in case of rain.

Additional improvements should result from a more careful processing of the reconstructed velocity field. Indeed, sector blanking of the lidar beam and optical anomalies in the lidar return lead to velocity jumps that cause large Lagrangian particle separation over the lidar cone. This in turn may lead to spurious FTLE ridges, some of which trigger false alarms under the PFG algorithm. The development of a high-end filtering methodology that eliminates spurious velocity jumps is currently underway.

Acknowledgments. H. A. K. was partially supported by a McGill MEDA. G. H. was partially supported by the Canadian National Science and Engineering Research Council under Grant 401839-11. This work builds on an initial study supported by the U.S. Air Force Office of Scientific Research under Grant FA9550-06-1-0092.

REFERENCES

- Chan, P. W., 2010: Lidar-based turbulence intensity calculation using glide-path scans of the Doppler light detection and ranging (lidar) systems at the Hong Kong International Airport and comparison with flight data and a turbulence alerting system. *Meteor. Z.*, **19**, 549–563.
- , and A. M. Shao, 2007: Depiction of complex airflow near Hong Kong International Airport using a Doppler lidar with a two-dimensional wind retrieval technique. *Meteor. Z.*, **16**, 491–504.
- , and Y. F. Lee, 2012: Application of short-range lidar in wind shear alerting. *J. Atmos. Oceanic Technol.*, **29**, 207–220.
- , C. M. Shun, and K. C. Wu, 2006: Operational lidar-based system for automatic windshear alerting at the Hong Kong International Airport. Preprints, *12th Conf. on Aviation, Range, and Aerospace Meteorology*, Atlanta, GA, Amer. Meteor. Soc., 6.11. [Available online at https://ams.confex.com/ams/Annual2006/techprogram/paper_100601.htm.]
- Farazmand, M., and G. Haller, 2012: Erratum and addendum to “A variational theory of hyperbolic Lagrangian coherent structures” [Physica D 240 (2011) 574–598]. *Physica D*, **241**, 439–441.
- Fawcett, T., 2006: An introduction to ROC analysis. *Pattern Recognit. Lett.*, **27**, 861–874.
- Fujita, T. T., 1978: Manual of downburst identification for Project NIMROD. SMRP Research Paper 156, University of Chicago, 104 pp.
- Haller, G., 2001: Distinguished material surfaces and coherent structures in three-dimensional fluid flows. *Physica D*, **149**, 248–277.
- , 2011: A variational theory of hyperbolic Lagrangian coherent structures. *Physica D*, **240**, 574–598.
- , and F. J. Beron-Vera, 2012: Geodesic theory of transport barriers in two-dimensional flows. *Physica D*, **241**, 1680–1702.
- Haynes, A., 1980: Description of a program developed for the analysis of windshears experienced during aircraft approach to landing. Royal Aircraft Establishment Tech. Memo. FS 321, 25 pp.
- ICAO, 2005: Manual on low-level windshear and turbulence. Doc 9817, AN/449, 1st ed. International Civil Aviation Organization, 222 pp.
- Jones, J. G., and A. Haynes, 1984: A peak-spotter program applied to the analysis of increments in turbulence velocity. Royal Aircraft Establishment Tech. Rep. 84071, 76 pp.
- Ottino, J. M., 1997: *The Kinematics of Mixing: Stretching, Chaos, and Transport*. Cambridge University Press, 364 pp.
- Peacock, T., and J. Dabiri, 2010: Introduction to focus issue: Lagrangian coherent structures. *Chaos*, **20**, 017501, doi:10.1063/1.3278173.
- Proctor, F. H., D. A. Hinton, and R. L. Bowles, 2000: A windshear hazard index. Preprints, *Ninth Conf. on Aviation, Range, and Aerospace Meteorology*, Orlando, FL, Amer. Meteor. Soc., 7.7. [Available online at https://ams.confex.com/ams/Sept2000/techprogram/paper_16347.htm.]
- Shun, C. M., and S. Y. Lau, 2002: Implementation of a Doppler light detection and ranging (lidar) system for the Hong Kong International Airport. Preprints, *10th Conf. on Aviation, Range, and Aerospace Meteorology*, Portland, OR, Amer. Meteor. Soc., 8.3. [Available online at https://ams.confex.com/ams/13ac10av/techprogram/paper_39018.htm.]
- , and P. W. Chan, 2008: Applications of an infrared Doppler lidar in detection of wind shear. *J. Atmos. Oceanic Technol.*, **25**, 637–655.
- Tang, W., P. W. Chan, and G. Haller, 2010: Accurate extraction of Lagrangian coherent structures over finite domains with application to flight data analysis over Hong Kong International Airport. *Chaos*, **20**, 017502, doi:10.1063/1.3276061.
- , —, and —, 2011a: Lagrangian coherent structure analysis of terminal winds detected by lidar. Part I: Turbulence structures. *J. Appl. Meteor. Climatol.*, **50**, 325–338.
- , —, and —, 2011b: Lagrangian coherent structure analysis of terminal winds detected by lidar. Part II: Structure evolution and comparison with flight data. *J. Appl. Meteor. Climatol.*, **50**, 2167–2183.